nature communications

Article

https://doi.org/10.1038/s41467-025-56065-9

Room temperature ferroelectricity in monolayer graphene sandwiched between hexagonal boron nitride

Received: 2 June 2024

Accepted: 8 January 2025

Published online: 30 January 2025

Check for updates

Fanrong Lin[1,6], Xiaoyu Xuan[1,6], Zhonghan Cao[2,6], Zhuhua Zhang[1] ✉, Ying Liu[1], Minmin Xue[1], Yang Hang[3], Xin Liu[1], Yizhou Zhao[1], Libo Gao[4], Wanlin Guo[1] ✉ & Yanpeng Liu[1,5] ✉

The ferroelectricity in stacked van der Waals multilayers through interlayer sliding holds great promise for ultrathin high-density memory devices, yet mostly subject to weak polarization and cryogenic operating condition. Here, we demonstrate robust room-temperature ferroelectricity in monolayer graphene sandwiched between hexagonal boron nitride layers with a rhombohedral-like stacking (*i.e.*, ABC-like stacking). The system exhibits an unconventional negative capacitance and record high electric polarization of 1.76 μC/cm^2 among reported sliding ferroelectrics to date. The ferroelectricity also exists in similarly sandwiched bilayer and trilayer graphene, yet the polarization is slightly decreased with odd-even parity. Ab initio calculations suggest that the ferroelectricity is associated with a unique switchable co-sliding motion between graphene and adjacent boron nitride layer, in contrast to existing conventional vdW sliding ferroelectrics. As such, the ferroelectricity can sustain up to 325 K and remains intact after 50000 switching cycles in ~300000 s duration at 300 K. These results open a new opportunity to develop ultrathin memory devices based on rhombohedral-like heterostructures.

The in-plane sliding of one two-dimensional (2D) material over another in vdW stacked layers of a non-centrosymmetric configuration can switch the out-of-plane ferroelectricity due to incomplete compensation of interlayer electric dipoles, known as sliding ferroelectrics[1–8]. This unique rationale enables mechanically robust ferroelectrics by leveraging the intralayer stiffness and interlayer slipperiness of 2D materials, while also ensuring electrical reliability through decoupling of electric polarization and in-plane conductivity[1,3,8–11]. Structurally different from conventional oxide ferroelectrics with enhanced depolarization during scaling down[12], sliding ferroelectrics showcase strikingly stable and switchable electric dipoles down to few and bilayer limit. Therefore, a visionary goal of sliding ferroelectrics is to serve in future high-density memory technology, but with the preconditions of sufficiently large polarization and thermal stability under practical operations[13–15].

The sliding ferroelectrics emerge typically in rhombohedral-stacked bilayers that are assembled in a parallel lattice orientation, for instance, parallel-stacked 2D transition metal dichalcogenides including WSe_2, $MoSe_2$, WS_2, MoS_2 and WTe_2, where each layer is offset by one third of a unit cell[6–11]. The broken inversion symmetry and polar stacking

[1]Key Laboratory for Intelligent Nano Materials and Devices of Ministry of Education, State Key Laboratory of Mechanics and Control of Mechanical Structures, and Institute for Frontier Science, Nanjing University of Aeronautics and Astronautics, Nanjing, China. [2]Zhangjiang Laboratory, Shanghai, China. [3]School of Flexible Electronics (Future Technologies) & Institute of Advanced Materials (IAM), Nanjing Tech University (Nanjing Tech), Nanjing, China. [4]National Laboratory of Solid State Microstructures, School of Physics, Collaborative Innovation Center of Advanced Microstructures, Nanjing University, Nanjing, China. [5]National Key Laboratory of Microwave Photonics, Nanjing University of Aeronautics and Astronautics, Nanjing, China. [6]These authors contributed equally: Fanrong Lin, Xiaoyu Xuan, Zhonghan Cao. ✉e-mail: chuwazhang@nuaa.edu.cn; wlguo@nuaa.edu.cn; chmliuyp@nuaa.edu.cn

order in such bilayer architecture further enable the engineering of sliding ferroelectrics even based on several constituents that are non-ferroelectric or non-polar in bulk, for example, hexagonal boron nitride (hBN)[4,5]. Further encapsulation of bilayer graphene by two hBN flakes at certain crystallographic alignment triggers unconventional ferroelectricities but with inadequate polarization value at room temperature[16–18]. In addition, the finite uncompensated charge density and limited superlattice size in aforementioned bilayers, restrict the upper limit of ferroelectric polarization and corresponding robustness[3,19,20].

In this Article, we propose a rhombohedral-like three-layer that consists top hBN layer, central graphene and bottom hBN layer for achieving robust room-temperature ferroelectricity, termed as oblique-stacked heterostructure (OSH) (Fig. 1a) in which boron atom, carbon atom and the empty site of hexagonal center from three individual layers are vertically aligned (B-C-h stacking, left panel in Fig. 1a). In this configuration, the inversion and mirror reflection symmetries are broken, resulting in a positive polarization P_+ in this domain[5]. Microscopically, the unequal p_z orbital couplings at two graphene flanks, the distorted C orbital binding with B orbital gives rise to an out-of-plane polarization. The third hBN layer that vertically aligns its hexagon lattice center sequentially with C and B atoms is of great importance to stabilize the stacking order. Stimulated by a moderate electric field, both graphene and top hBN layer synergistically slides to form reversely polarized h-C-B stacking (right panel in Fig. 1a).

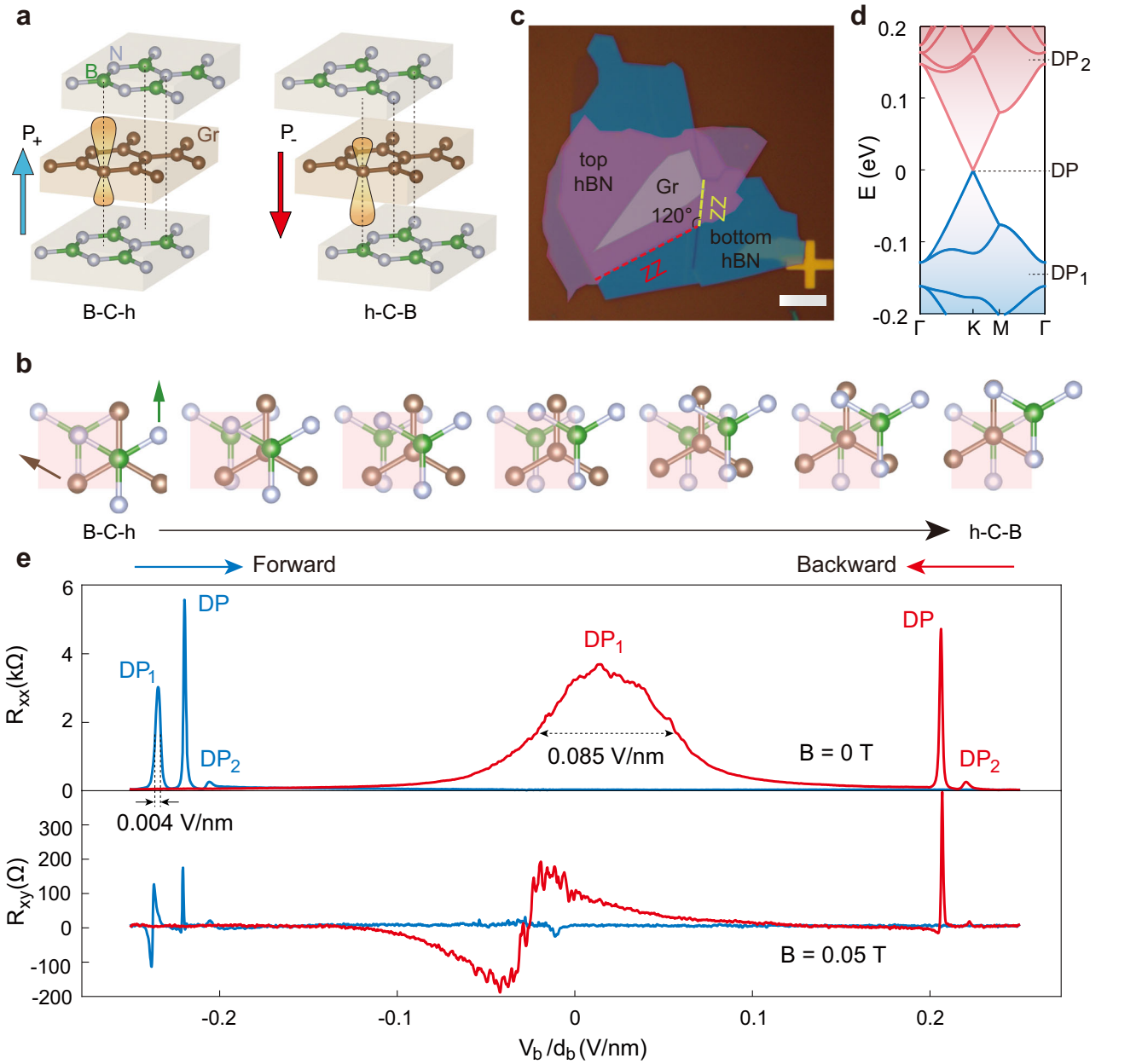

Fig. 1 | Electric hysteresis of the OSH device 1. a Atomic structure of the OSHs at two metastable states. **b** Structural evolution of the OSHs under co-sliding motions of graphene and hBN. White, gray and green spheres denote N, C and B atoms, respectively. Pink background marks the stationary bottom hBN layer while graphene and top hBN layers co-slide during ferroelectric switch. Brown and green arrows mark the sliding direction of graphene and hBN, respectively. **c** An optical image of one OSH stack. Scale bar: 10 μm. The zigzag edges of top and bottom hBN flakes are marked by red and yellow dashed lines, respectively. **d** Band structure of graphene/hBN heterolayer with zero twist angle. In the OSH device 1, the graphene electronic band is folded by graphene/hBN moiré superlattice potential, which clones the Dirac point (DP) at the superlattice band edges, termed as secondary Dirac points DP_1 and DP_2, respectively (below and above the main DP, Fig. 1d)[23]. **e** Top: four-probe longitudinal resistance R_{xx} of OSH device 1 during forward (blue) and backward (red) sweeps of back-gate voltages, at $T = 1.5$ K. Bottom: Hall resistance R_{xy} hysteresis at $B = 0.05$ T.

Figure 1b shows the proposed co-sliding path from ab initio calculations (see Fig. S1-S3 for detailed discussions). The polar domains expand (shrink) with the applied electric fields to reach the minimum energy, resulting in net out-of-plane polarizations. Compared to the traditional bilayer ferroelectrics, the superlubric graphene/hBN hetero-interface with minor lattice mismatch[21] and enlarged moiré superlattice size[22] leads to strong polarizations with ultralow coercive fields[11], while the relatively higher barrier of co-sliding motion here assures the out-of-plane polarization persisting up at and beyond room temperature.

Results and discussion

To precisely achieve the OSHs, we developed a flip and reflection transfer method (see Supplementary Fig. S4), which actualizes the parallel alignment of B(N)-terminated zigzag edge of one hBN, graphene zigzag edge and B(N)-terminated zigzag edge of other hBN (Fig. 1c). Figure 1e displays the measured longitudinal resistance R_{xx} against the bottom electric field V_b/d_b during the forward and backward sweeps of back-gate voltage V_b. Upon forward sweep, the Fermi level shifts upward from a position below a secondary Dirac point DP_1, the main Dirac point DP to a position above another secondary Dirac point DP_2 (Fig. 1d)[23]. Three resistance peaks are sequentially observed at $V_b/d_b = -0.235$, -0.220, and -0.205 V/nm when the Fermi level crosses the DP_1, DP and DP_2, respectively; whereas during the backward sweep they shift to 0.221, 0.206, and 0.014 V/nm, respectively. The sharp peaks during the unidirectional gate sweep indicate a single domain configuration for charge polarization with a sample-wide homogeneity. The pronounced electrical hysteresis is a hallmark of intrinsic ferroelectricity, which is re-confirmed by the measured R_{xy} whose sign depends on the charge polarity (Fig. 1e, bottom). In addition, the hysteresis features are robust after ramping the temperature up to 300 K (see Supplementary Fig. S5–S10).

The oblique-stacking configuration is central to realize and stabilize the ferroelectricity in such three-layer heterostructure. For verifications, we further fabricated extra hBN/graphene/hBN three-layer devices in different stacking configurations (Table S1): (i) two parallel-aligned hBN flakes but with graphene twisted by ~2° (device 2) (see Supplementary Fig. S11–S15), (ii) two anti-parallel aligned hBN flakes (flip without reflection) but with graphene aligned (device 3) (see Supplementary Fig. S16-S17) and (iii) completely misaligned hBN/graphene/hBN stack (device 4) (see Supplementary Fig. S18). The ferroelectricity vanishes in non-OSH device 3 and device 4, revealing the necessity of oblique-stacking in generating ferroelectricity in hBN/graphene/hBN systems. Considering two variable stacking surfaces (A and A') of AA'-stacked bulk hBN, two options for hBN's principal edges (armchair and zigzag), and two options for zigzag edges, the possibility of realizing OSHs in the occasionally aligned hBN/graphene/hBN stack for inducing ferroelectricity is only 1/8. This may explain why no ferroelectricity has been reported previously in such a simple system. By developing a new transfer method that involves controllable flip and reflection of hBN multilayers, we have achieved 100% productivity of OSHs demonstrating similar ferroelectric hysteresis behavior.

Negative capacitance and unconventional ferroelectric loop

To understand the ferroelectric hysteresis, we conducted magneto-transport measurements of the OSH device 1 by applying a vertical magnetic field B. Figure 2a presents the mapping of measured R_{xx} versus B and V_b/d_b under the forward sweep. The magnetic field-induced quantum Hall effect in graphene is manifested as linear Landau fans that follow the Streda formula $dn/dB = \upsilon e/h$ (where n is the carrier density in graphene, e the elementary charge, h the Planck constant, and υ the filling factor)[24]. The slope dV_b/dB for each Landau state should be a constant at a given υ, as described by a parallel

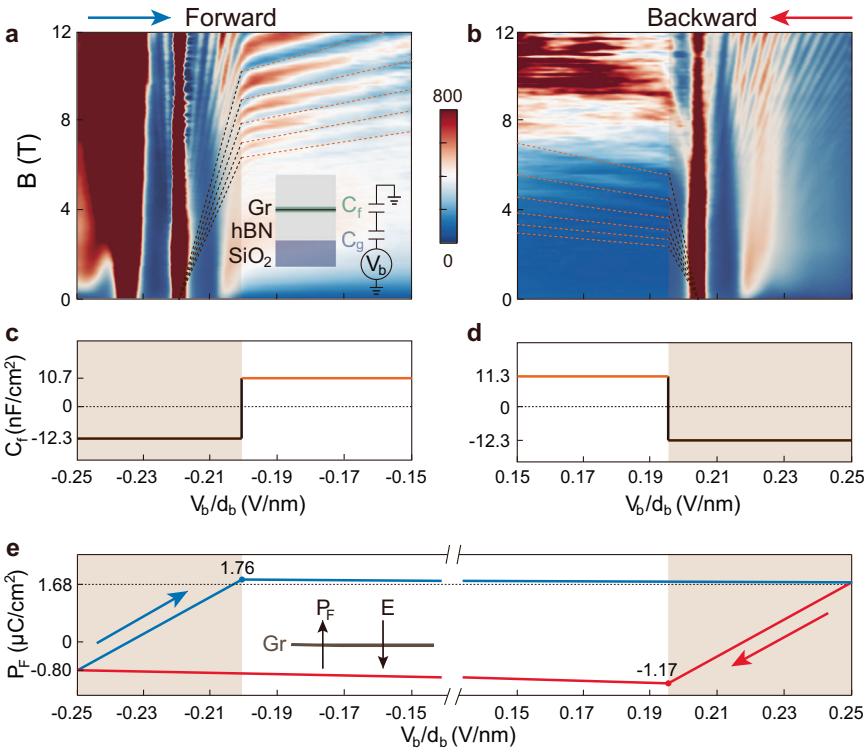

Fig. 2 | Ferroelectric capacitance of the OSH device 1. The four-probe resistance R_{xx} as functions of applied electric field (V_b/d_b) and magnetic field (B) during forward (**a**) and backward (**b**) sweeps of V_b. The inset illustrates the series-connected ferroelectric and geometric capacitances, i.e., C_f and C_g. $n = C_{tot}(V_b - V_b^0)$ and $C_g = \epsilon\epsilon_0/d_b$, V_b^0 is the V_b required to shift the Fermi level to the DP, ϵ_0 is the permittivity of vacuum, and $\epsilon = 4$ represents the relative permittivity. The extracted ferroelectric capacitances during forward (**c**) and backward (**d**) sweeps. Light gray-colored backgrounds highlight the negative capacitance regions. **e** The obtained polarization hysteresis loop. Arrows indicate the scanning directions of V_b/d_b. The inset sketches the mutual action of ferroelectric polarization P_F and electric field E.

capacitor model under a gate voltage. By contrast, we observe an abrupt change of slope dV_b/dB at $V_b/d_b = -0.20$ V/nm for each Landau state. The change in slope also arises at $V_b/d_b = 0.20$ V/nm during the backward sweep (Fig. 2b). As the quantum Hall oscillation depends only on n and B, these results suggest an abrupt change in the total capacitance C_{tot} that dictates how efficient V_b is to modulate n in graphene, differentiating from reported bilayer graphene/hBN devices[18]. As such, one could divide the gate-voltage modulation of R_{xx} into two regions, which are temporarily assigned as the high-capacitance and low-capacitance regions.

The abrupt change in capacitance reflects the reversal of ferroelectric polarization during the sweep of V_b. To shed light on this point, we modify the parallel capacitor model by considering a series connection of a capacitance C_f induced by the ferroelectricity and a common geometric capacitance of back-gate C_g (Fig. 2a, inset). The total capacitance C_{tot} reads as $(C_g^{-1} + C_f^{-1})^{-1}$, we can isolate the contribution of C_f from C_{tot} based on the observed Landau fans. C_f turns out to be −12.3 nF/cm^2 in the high-capacitance region and 10.7 nF/cm^2 in the low-capacitance region for the forward sweep (Fig. 2c); the corresponding values are −12.3 and 11.3 nF/cm^2 for the backward sweep, respectively (Fig. 2d). The negative C_f results in a 16-fold increase of C_{tot} with respect to C_g alone. As a result, the back-gate modulation to carrier density n is efficient in negative C_f region yet highly sluggish in the region of positive C_f. This phenomenon is also supported by the results shown in Fig. 1d, where three R_{xx} peaks (in the region of negative C_f) exhibit a full-width at half maximum of only 0.004 V/nm in forward sweep while that of the DP_1 peak (in the region of positive C_f) is broadened to 0.085 V/nm in backward sweep. The negative capacitance further verifies the ferroelectricity in the sandwiched graphene heterostructure, as has been used for proving ferroelectricity in $Pb(Zr_{0.2}Ti_{0.8})O_3$[25] and $Hf_{0.5}Zr_{0.5}O_2$[26].

The out-of-plane ferroelectric polarization P_F can be determined based on the carrier density n in graphene through $D = P_F + E = ne$, where D represents the displacement field comprising P_F and electric field E (Fig. 2e, inset). According to the n derived from the Landau fan diagram, we obtain the electric field-dependent P_F that forms a unique parallelogram-shaped hysteresis loop (Fig. 2e). When V_b/d_b is swept forward from -0.25 V/nm, P_F linearly increases from a reversely saturated -0.8 μC/cm^2 and reaches a saturated value of +1.76 μC/cm^2 at −0.20 V/nm, significantly larger than all reported values in previous sliding ferroelectrics. The inequivalent positive and negative polarizations support our theory of co-sliding ferroelectric (see Supplementary Fig. S1). The electric field-dependent P_F evolves vice versa for the backward sweep and constitutes a closed hysteresis loop. Moreover, the linear dependence of P_F on V_b/d_b distinctly differs from the nonlinear behavior typically observed in conventional ferroelectrics[27], enabling a precise control over polarization-based electric properties.

Electric-field-dependent hysteresis behavior

To further disclose the unconventional ferroelectric loop, we conducted extensive measurements of R_{xx} against V_b/d_b sweeps from different, initial back-gate voltages V_b^{ini}. During the forward sweep

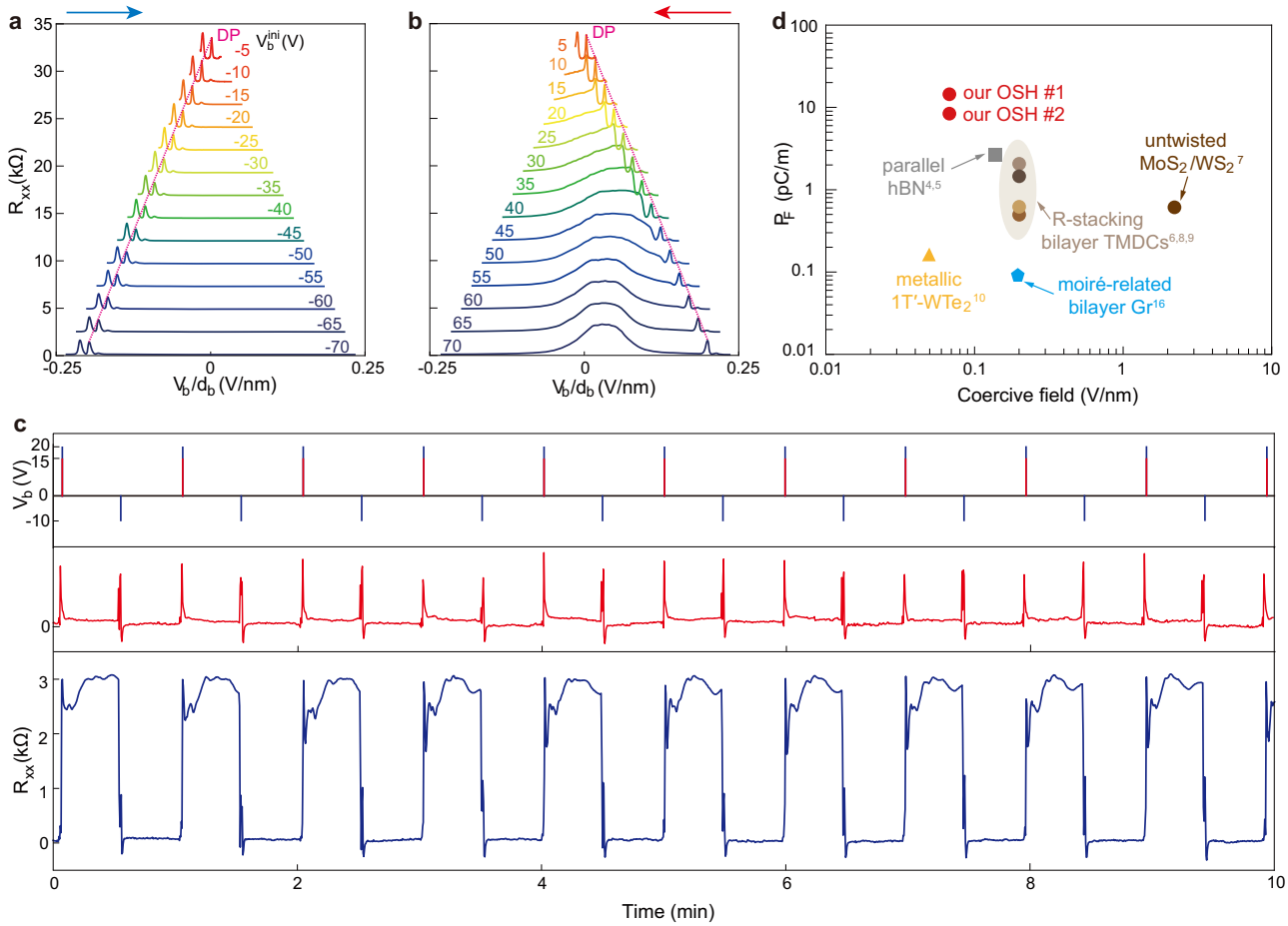

Fig. 3 | Gate-dependent ferroelectric switch. The four-probe resistance R_{xx} as a function of V_b/d_b during the forward (**a**) and backward (**b**) sweeps from different initial back-gate voltage V_b^{ini}. The Dirac point of each curve is marked and aligned by a pink dashed line. **c** R_{xx} under applied periodic electric pulses. The pulse interval is 0.5 min, respectively. Top: evolution of V_b with time. Middle: the responses of R_{xx} to the electric pulses of $V_b = 15$ V. Bottom: the responses of R_{xx} to the electric pulses with positive V_b of 20 V. The negative V_b is fixed at −10 V. **d** Electric polarization and coercive field of our OSH devices, compared to previous 2D ferroelectrics.

(Fig. 3a), three resistance peaks (DP_1, DP, and DP_2) were evenly spaced by 0.015 V/nm independent of V_b^{ini}, indicating that the negative C_f is involved in sensitively modulating n. However, as P_F is completely reversed, C_f becomes positive and the Fermi level turns to slowly shift with the applied V_b/d_b. As a result, the DP_1 peak is not only significantly broadened but also located at a nearly fixed position of 0.014 V/nm. When V_b^{ini} is below 20 V, P_F cannot be completely reversed even when the Fermi level starts to cross the DP_1, such that the negative C_f remains active in modulating n therein, leading to partial sharpening of the DP_1 peak on the right-hand side. As V_b^{ini} decreases further, the region influenced by negative C_f extends towards zero field since P_F gets farther from complete reversal, making the DP_1 peak increasingly sharpened (Fig. 3b). Our theoretical calculations suggest that such hysteresis behavior may stems from the ferroelectric lattice dynamics in hBN/Gr/hBN stacks (see Supplementary Fig. S19 for detailed description).

We then demonstrate the nonvolatile memory function by subjecting OSH device to a periodic pulse of V_b (Fig. 3c, top panel) and monitoring the corresponding variation in R_{xx}. Upon applying an electric pulse of $V_b = 20$ V, R_{xx} promptly transitions from its intrinsic value of approximately 3 Ω to 3 kΩ (Fig. 3c, bottom panel), dominated by the DP_1 peak (Fig. 3b). Periodic applications of positive and negative pulses robustly switch the OSH device between high and low resistance states for twenty consecutive cycles (see Supplementary Fig. S7), validating the inherent ferroelectric nature of OSHs. After reducing the electric pulse to $V_b = 15$ V, however, no sustainable high resistance state is achieved since this voltage does not sufficiently saturate P_F for forming a stable polar state. The threshold V_b/d_b for switching the electric transport is taken as the coercive field of P_F, which is respectively determined to be 0.067 and -0.033 V/nm for positive and negative coercive fields (see Supplementary Fig. S8). These coercive fields are several times lower than the value of ~0.2 V/nm in rhombohedral stacked bilayer TMDs[9] and 0.08-0.20 V/nm in doped HfO_2 films[28,29].

Figure 3d compares the P_F and coercive field of our OSH devices with those of previously reported sliding ferroelectrics. Our determined P_F of ~12 pC/m (1.76 μC/cm² × 0.68 nm, by taking the spacing of 0.68 nm between two hBN layers as the dipole separation) is significantly larger than the values in all sliding ferroelectrics, e.g., 2.25 pC/m in stacked hBN bilayers[4], 0.6 pC/m in marginally twisted MoS_2[8], 0.12 pC/m in bilayer graphene superlattice[16]. Notably, this value lies in the same order of magnitude as the remanent polarization ranging from 1-10 μC/cm² in Si-doped HfO_2 nanofilms[30]. In addition, our OSH device exhibits lower coercive fields only secondary to that of semimetallic 1 T′-WTe_2 bilayers[10].

Layer-dependent polarizations and corresponding robustness

To re-validate this robust vdW ferroelelctric, we further fabricated two multilayer OSHs by replacing monolayer graphene with Bernal bilayer and trilayer graphene. Figure 4a shows the Hall carrier density [$n_{Hall} = B/(eR_{xy})$] of OSH device 5 with bilayer graphene under forward/backward back-gate scans. The parallelogram-shaped loop with two capacitance regions is clearly observed during each unidirectional scan. After converting n_{Hall} to P_F (Fig. 4b), the positive (negative) ferroelectric polarization P_F is determined to be 0.81 μC/cm² (-0.55 μC/cm²), one half of the values of monolayer-graphene-basis OSHs. In this B-C-C-h stacking order (Fig. 4c), unlike the B-C-h stacking case where the inversion symmetry is completely broken, opposite charge polarization occurs at dual graphene/hBN interfaces (see Supplementary Fig. S20–S21), resulting in a reduced and reversed net polarization. The directions of polarizations are determined by calculating the electrostatic energy profile of each stacking configuration (see Supplementary Fig. S1).

Interestingly, the ferroelectric polarization of OSH device 6 based on trilayer graphene (Fig. 4d, e) increase up to $P_F = 1.22$ μC/cm², right in between two values of monolayer- and bilayer-graphene OSH devices. With respect to monolayer-graphene-basis OSHs, two graphene/hBN interfaces (Fig. 4f) are mirrorly asymmetric and their couplings become lower because of wider separation, hence reducing the total polarization. Compared with bilayer graphene OSHs, meanwhile, the inversion symmetry of trilayer graphene breaks (see Supplementary Fig. S22–S24) and leads to a relatively larger polarization.

We finally test the robustness of ferroelectric switching behavior against magnetic field, electrical stimuli and elevated temperature. At $T = 300$ K and $B = 1$ T, the n_{Hall} with respect to V_b/d_b (Fig. 4h) maintains a well-defined parallelogram-shaped loop at varying initial back-gate voltages V_b^{ini}. The corresponding negative capacitance maintains a constant value of -12.7 nF/cm² in the temperature ranging from 100 K to 300 K (see Supplementary Fig. S25). The gate-dependent polarization and hysteretic behavior allow us to write and read the polarization in a nonvolatile way. After 50,000 write/read cycles, the hall resistances at two states (Fig. 4i) fully recovery and maintain well-defined square waves. The positively charged state can steadily persist for 24 hours after voltage withdrawal but can be instantaneously switched back to the negatively charged state upon application of a negative pulse (See supplementary Fig. S26). It is recognized that the actual memory devices usually work beyond room temperature (for example, 325 K) because of massive heat dissipations. Interestingly, the switching behavior of our ferroelectric device are well duplicated after tens of consecutive pulses at 325 K (see Supplementary Fig. S27), demonstrating itself a potential building block for miniaturized memory devices.

In summary, we have demonstrated monolayer graphene-basis OSH device that exhibits robust room-temperature ferroelectricity up to ~1.76 μC/cm², several times higher than the reported values in all sliding ferroelectrics, while the coercive field of ~0.07 V/nm can be three times lower. In contrast to conventional metal-oxide-basis ferroelectrics, the ultrathin ferroelectric system composed of graphene and hBN avoids formation of parasitic SiO_x layers and any degradation during classical silicon processing, becoming an good alternatives in densely integrated electronics[31]. Our experimental clues of odd-even parity may substantially expand 2D ferroelectricity boundaries by constructing alternative graphene and hBN stacks and even tandem OSHs. Moving forward, with the successful growth of wafer-scale and single-crystalline graphene[32] and boron nitride[33], the trinity of robust hysteresis, remarkable controllability and high mobility in the unconventional ferroelectrics opens a wealthy of opportunities for developing ultrathin devices with superior performance.

Methods

Device fabrications

Graphene and hexagonal boron nitride (hBN) were respectively exfoliated on SiO_2 (285 nm)/Si wafer by blue 'magic' tapes (ELP BT-150E-KL). The graphene and hBN flakes with sharp and straight edges were localized under optical microscope and the edges were analyzed by Raman spectroscope to determine whether it follows the armchair or zigzag lattice orientation[34]. After that, graphene and hBN were assembled into the hBN/graphene/hBN heterostructure in argon-filled glovebox via our well-established flip and reflection transfer method (see Supplementary Note S4 for details). The final stacks were thermally annealed at $T = 200$ °C for 48 h in an ultrahigh vacuum (~ 5×10^{-10} mbar) chamber.

Configurations of different devices

(1) For OSH device 1, the hBN/monolayer-graphene/hBN heterostructure was perfectly double-aligned in which the zigzag lattice orientations of both hBN flakes and graphene were precisely aligned.

(2) For device 2, top hBN and bottom hBN were parallel-stacked, but the sandwiched monolayer graphene was slightly twisted by an angle of ~2°.

https://doi.org/10.1038/s41467-025-56065-9

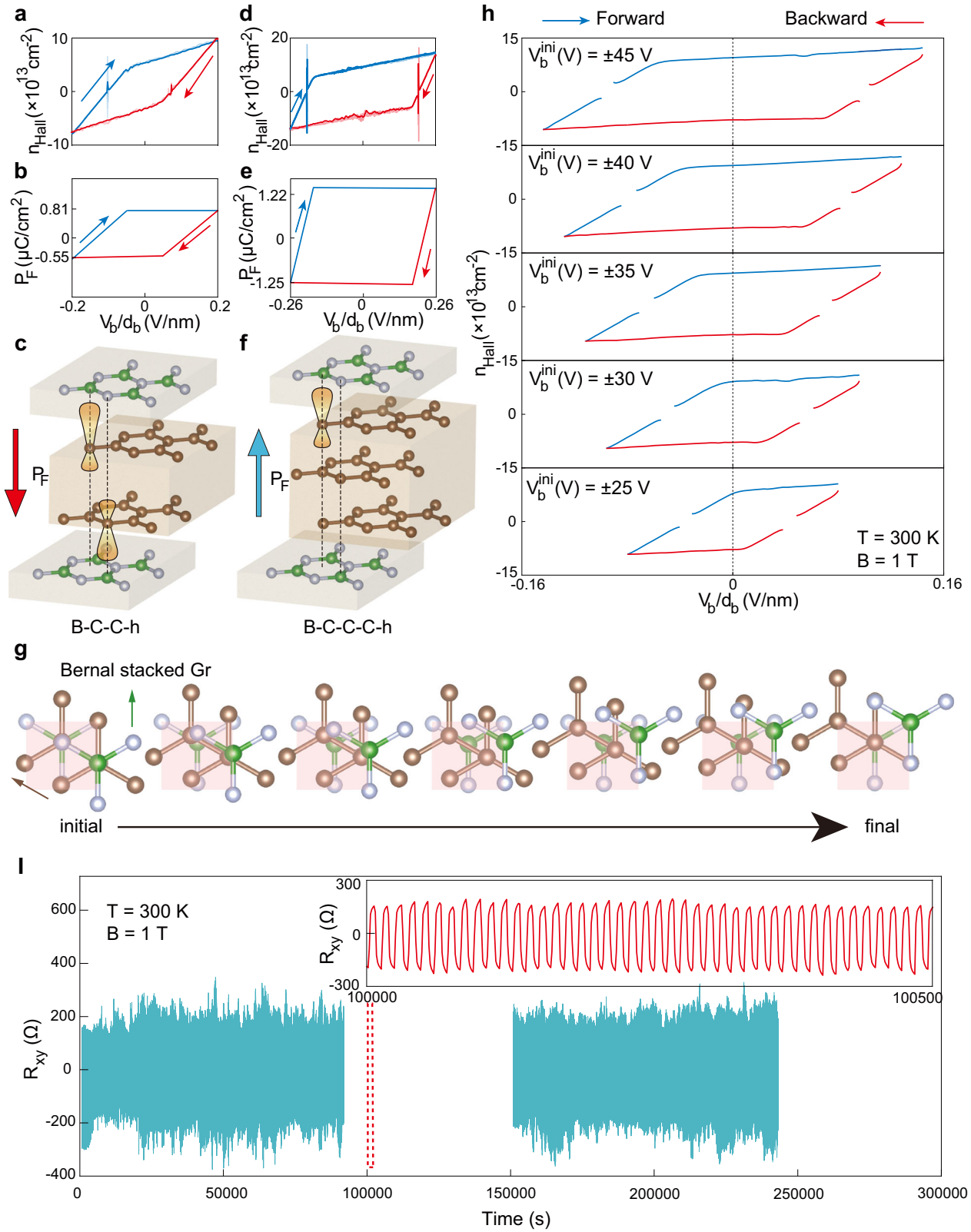

Fig. 4 | Robust hysteresis and ferroelectric switching in multilayer OSH devices with Bernal bilayer and trilayer graphene. a n_{Hall} as a function of V_b/d_b during forward (blue) and backward (red) sweeps in OSH device 5. **b** The extracted polarization hysteresis loop of OSH device 5. **c** Atomic illustration of OSH device 5 showing the parallel-orientation of bilayer graphene and top/bottom hBN layers. The local registry with vertical B-C-C-h alignment possesses a negative polarization. **d** The n_{Hall} vs V_b/d_b loop of OSH device 6 with trilayer graphene. **e** The polarization hysteresis loop of device 6. **f** The atomic arrangement of the OSHs based on trilayer graphene with vertical B-C-C-C-h alignment. **g** Structural evolution of the OSHs under co-sliding motions of Bernal stacked multilayer graphene and hBN. Pink background marks the stationary bottom hBN layer. Brown and green arrows mark the sliding direction of graphene and hBN, respectively. **h** n_{Hall} hysteresis loops of OSH device 6 under different V_b^{ini} at $T = 300$ K. **i** The R_{xy} response of OSH device 6 under 50,000 electric pulses ($V_b = +20/-20$ V) at $T = 300$ K & $B = 1$ T. Inset is the close-view of 87 switches within 500 s.

(3) For non-OSH device 3, the top hBN, graphene and bottom hBN were aligned with zero twist. The device was fabricated via a flip without reflection method, the top and bottom hBN flakes were antiparallel-stacked.

(4) For device 4, monolayer graphene and two hBN flakes were completely misaligned.

(5) For OSH device 5, top hBN, Bernal bilayer graphene and bottom hBN were oblique-stacked that produce a vertical B-C-C-h alignment.

(6) For OSH device 6, top hBN, Bernal trilayer graphene and bottom hBN were oblique-stacked, in which vertical B-C-C-C-h alignment of five layers was formed.

Transport measurement

The transport measurements were conducted in a TeslatronPT system (Oxford Instrument) with a base temperature of ~1.5 K. Four-probe measurement was conducted by using lock-in amplifiers (Stanford Research systems: SR830) with a frequency 13.373 Hz and a constant source-drain current of 100 nA. The pulse measurements were conducted by using Keithley 2400 for voltage supply and Keithley 2000 for voltage measurement.

Tight binding calculation

The moiré bands were calculated using a tight-binding model by considering only the p_z orbitals. The Hamiltonian is written as:

$$H = -\sum_{i,j} T(R_i - R_j)|R_i\rangle\langle R_j| + \sum_i V(R_i)|R_i\rangle\langle R_j|, \quad (1)$$

where R_i represents the lattice point at atom site i. $V(R_i)$ is the on-site energy on site i. we assume $V_C = 0$ for carbon atoms, $V_B = 3.34$ eV for boron atoms and $V_N = -1.40$ eV for nitrogen atoms, respectively. $T(R_i\text{-}R_j)$ is the transfer integral between sites i and j and is simply built with the common Slater-Koster-type function:

$$\begin{aligned} T(R) &= V_{pp\pi}\left[1 - \left(\frac{R_z}{R}\right)^2\right] + V_{pp\sigma}\left(\frac{R_z}{R}\right)^2, \\ V_{pp\pi} &= V^0_{pp\pi}\exp\left(-\frac{R-a_0}{r_0}\right), \\ V_{pp\sigma} &= V^0_{pp\sigma}\exp\left(-\frac{R-d_0}{r_0}\right). \end{aligned} \quad (2)$$

Here, R_z is the z-component of the distance R, $a_0 \approx 0.142$ nm is the distance of nearest-neighbor atoms in graphene, and d_0 is the interlayer spacing of graphene. $V_{pp\pi}$ and $V_{pp\sigma}$ are the transfer integrals between the nearest-neighbor atoms of monolayer graphene and the vertically located atoms on the neighboring layers. We adopt $V_{pp\pi} \approx -2.7$ eV and $V_{pp\sigma} \approx 0.48$ eV to fit the dispersions of graphene. $r_0 \approx 0.45$ nm is the decay length of the transfer integral[35].

Ab initio calculations

The calculations were conducted employing the density functional theory within the VASP code[36,37]. The exchange-correlation functional utilized was the Perdew-Burke-Ernzerhof (PBE) functional generalized gradient approximation[38]. To account for core electrons, the projector augmented wave method was employed[39]. A vacuum region with a width of 15 Å was introduced to the models to effectively isolate adjacent periodic images. The kinetic cutoff energy for plane-waves was set at 500 eV, and for two-dimensional models, a simple 24 × 24 × 1 k-point mesh was employed for the Brillouin zone. The relaxation of atomic structures was carried out until the force on each atom dropped below 0.01 eV/Å, and energy convergence was aimed at 10^{-5} eV. To capture dispersive forces, the advanced optB86b-vdW method was integrated[40,41], and for crystalline polarization evaluation, the Berry-phase method was adopted[42]. Differential charge density is calculated using the total charge density of the system subtracting the charge density of each constituent part layer. The ferroelectric switching pathways were calculated by the nudged elastic band (NEB) method[43] with a cutoff energy of 500 eV and with the force on each atom being less than 0.2 eV/Å. The other parameters for the NEB calculation were set to default values.

Data availability

The authors declare that all data supporting the findings of this study are presented in the article and Supplementary Information or are available from the corresponding author upon reasonable request. The data is available in the Source Data file. Source data are provided with this paper.

References

1. Li, L. & Wu, M. H. Binary compound bilayer and multilayer with vertical polarizations: Two-dimensional ferroelectrics, multiferroics, and nanogenerators. *ACS Nano* **11**, 6382–6388 (2017).
2. Yang, L., Ding, S. P., Gao, J. H. & Wu, M. H. Atypical sliding and moire ferroelectricity in pure multilayer graphene. *Phys. Rev. Lett.* **131**, 096801 (2023).
3. Ji, J. Y., Yu, G. L., Xu, C. S. & Xiang, H. J. General theory for bilayer stacking ferroelectricity. *Phys. Rev. Lett.* **130**, 146801 (2023).
4. Yasuda, K., Wang, X. R., Watanabe, K., Taniguchi, T. & Jarillo-Herrero, P. Stacking-engineered ferroelectricity in bilayer boron nitride. *Science* **372**, 1458–1462 (2021).
5. Stern, M. V. et al. Interfacial ferroelectricity by van der waals sliding. *Science* **372**, 1462–1466 (2021).
6. Deb, S. et al. Cumulative polarization in conductive interfacial ferroelectrics. *Nature* **612**, 465–469 (2022).
7. Rogee, L. et al. Ferroelectricity in untwisted heterobilayers of transition metal dichalcogenides. *Science* **376**, 973–978 (2022).
8. Weston, A. et al. Interfacial ferroelectricity in marginally twisted 2d semiconductors. *Nat. Nanotechnol.* **17**, 390–395 (2022).
9. Wang, X. R. et al. Interfacial ferroelectricity in rhombohedral-stacked bilayer transition metal dichalcogenides. *Nat. Nanotechnol.* **17**, 367–371 (2022).
10. Fei, Z. Y. et al. Ferroelectric switching of a two-dimensional metal. *Nature* **560**, 336–339 (2018).
11. Ko, K. H. Y. et al. Operando electron microscopy investigation of polar domain dynamics in twisted van der waals homobilayers. *Nat. Mater.* **22**, 992–998 (2023).
12. Junquera, J. & Ghosez, P. Critical thickness for ferroelectricity in perovskite ultrathin films. *Nature* **422**, 506–509 (2003).
13. Khan, A. I., Keshavarzi, A. & Datta, S. The future of ferroelectric field-effect transistor technology. *Nat. Electron.* **3**, 588–597 (2020).
14. Wang, Z. R. et al. Resistive switching materials for information processing. *Nat. Rev. Mater.* **5**, 173–195 (2020).
15. Noheda, B., Nukala, P. & Acuautla, M. Lessons from hafnium dioxide-based ferroelectrics. *Nat. Mater.* **22**, 562–569 (2023).
16. Zheng, Z. R. et al. Unconventional ferroelectricity in moiré heterostructures. *Nature* **588**, 71–76 (2020).
17. Niu, R. R. et al. Giant ferroelectric polarization in a bilayer graphene heterostructure. *Nat. Commun.* **13**, 6241 (2022).
18. Yan, X. D. et al. Moiré synaptic transistor with room-temperature neuromorphic functionality. *Nature* **624**, 551–556 (2023).
19. Wang, C. S., You, L., Cobden, D. & Wang, J. L. Towards two-dimensional van der waals ferroelectrics. *Nat. Mater.* **22**, 542–552 (2023).
20. Zhang, D. W., Schoenherr, P., Sharma, P. & Seidel, J. Ferroelectric order in van der waals layered materials. *Nat. Rev. Mater.* **8**, 25–40 (2023).
21. Song, Y. M. et al. Robust microscale superlubricity in graphite/hexagonal boron nitride layered heterojunctions. *Nat. Mater.* **17**, 894–899 (2018).
22. Andelkovic, M., Milovanovic, S. P., Covaci, L. & Peeters, F. M. Double moiré with a twist: Supermoire in encapsulated graphene. *Nano Lett.* **20**, 979–988 (2020).

23. Ponomarenko, L. A. et al. Cloning of Dirac fermions in graphene superlattices. *Nature* **497**, 594–597 (2013).
24. MacDonald, A. The quantum Hall effects. In *Quantum Coherence in Mesoscopic Systems*, (ed. Kramer, B.) 195-217 (Springer, 1991).
25. Khan, A. I. et al. Negative capacitance in a ferroelectric capacitor. *Nat. Mater.* **14**, 182–186 (2015).
26. Hoffmann, M. et al. Unveiling the double-well energy landscape in a ferroelectric layer. *Nature* **565**, 464–467 (2019).
27. Wang, Y. et al. A stable rhombohedral phase in ferroelectric $Hf(Zr)_{1+x}O_2$ capacitor with ultralow coercive field. *Science* **381**, 558–563 (2023).
28. Schroeder, U., Park, M. H., Mikolajick, T. & Hwang, C. S. The fundamentals and applications of ferroelectric HfO_2. *Nat. Rev. Mater.* **7**, 653–669 (2022).
29. Mikolajick, T., Slesazeck, S., Park, M. H. & Schroeder, U. Ferroelectric hafnium oxide for ferroelectric random-access memories and ferroelectric field-effect transistors. *MRS Bull.* **43**, 340–346 (2018).
30. Richter, C. et al. Si doped hafnium oxide-a "fragile" ferroelectric system. *Adv. Electron. Mater.* **3**, 1700131 (2017).
31. Kang, S. et al. Highly enhanced ferroelectricity in HfO_2-based ferroelectric thin film by light ion bombardment. *Science* **376**, 731–738 (2022).
32. Yuan, G. W. et al. Proton-assisted growth of ultra-flat graphene films. *Nature* **577**, 204–208 (2020).
33. Lee, J. S. et al. Wafer-scale single-crystal hexagonal boron nitride film via self-collimated grain formation. *Science* **362**, 817–821 (2018).
34. Lin, F. et al. Graphene binding on black phosphorus enables high on/off ratios and mobility. *Natl Sci. Rev.* **11**, nwad279 (2024).
35. Moon, P. & Koshino, M. Electronic properties of graphene/hexagonal-boron-nitride moiré superlattice. *Phys. Rev. B* **90**, 155406 (2014).
36. Kresse, G. & Hafner, J. Ab initio molecular-dynamics simulation of the liquid-metal-amorphous-semiconductor transition in germanium. *Phys. Rev. B* **49**, 14251–14269 (1994).
37. Kresse, G. & Furthmuller, J. Efficient iterative schemes for ab initio total-energy calculations using a plane-wave basis set. *Phys. Rev. B* **54**, 11169–11186 (1996).
38. Perdew, J. P., Burke, K. & Ernzerhof, M. Generalized gradient approximation made simple. *Phys. Rev. Lett.* **77**, 3865–3868 (1996).
39. Blochl, P. E. Projector augmented-wave method. *Phys. Rev. B* **50**, 17953–17979 (1994).
40. Klimes, J., Bowler, D. R. & Michaelides, A. Chemical accuracy for the van der waals density functional. *J. Phys. -Condes. Matter* **22**, 022201 (2010).
41. Klimes, J., Bowler, D. R. & Michaelides, A. Van der waals density functionals applied to solids. *Phys. Rev. B* **83**, 195131 (2011).
42. Kingsmith, R. D. & Vanderbilt, D. Theory of polarization of crystalline solids. *Phys. Rev. B* **47**, 1651–1654 (1993).
43. Henkelman, G., Uberuaga, B. P. & Jónsson, H. A climbing image nudged elastic band method for finding saddle points and minimum energy paths. *J. Chem. Phys.* **113**, 9901–9904 (2000).

Acknowledgements

We thank Prof. Jens Martin for fruitful discussions. We acknowledge the support provided by the National Natural Science Foundation of China (12304106, 12372111, 12261160367, 12225205, T2293691, 12104228, U2441272), the Natural Science Foundation of Jiangsu Province (BK20210312), the National Key Research and Development Program of China (2024YFA1409600), the Fundamental Research Funds for the Central Universities and the State Administration of Science, Technology and Industry for National Defense (NE2023006, NC2023001, NJ2023002, NJ2022002, ILF23010, THB24004), Research Fund of State Key Laboratory of Mechanics and Control of Mechanical Structures (MCMS-I-0422K01), a project funded by the Priority Academic Program Development of Jiangsu Higher Education Institutions, the Postdoctoral Science Foundation of Jiangsu Province (YBA21046), and the Jiangsu Funding Program for Excellent Postdoctoral Talent (2023ZB347). The computations were performed at the High-performance Computational Center at NUAA. Thanks to the Center for Microscopy and Analysis (NUAA) for technical assistance.

Author contributions

Y.P.L., W.G. and Z.Z supervised and designed the experiments. F.L., and Z.C. performed the experiments. Y.L., X.L., and Y.Z. helped with the device fabrication and measurements. Z.Z. designed and X.X., M.X., and Y.H. conducted the computations. F.L., X.X., Y.P.L., L.G., W.G. and Z.Z. analyzed the data. F.L., Y.P.L. and Z.Z. wrote the paper with input from all the co-authors.

Competing interests

The authors declare no competing interests.

Additional information

Supplementary information The online version contains supplementary material available at https://doi.org/10.1038/s41467-025-56065-9.

Correspondence and requests for materials should be addressed to Zhuhua Zhang, Wanlin Guo or Yanpeng Liu.

Peer review information *Nature Communications* thanks Zhi Yan and the other anonymous reviewer(s) for their contribution to the peer review of this work. A peer review file is available.